Physics and Chemistry of Minerals (2020) 47:25
https://doi.org/10.1007/s00269-020-01094-7

ORIGINAL PAPER

Crystal-chemical behavior of Fe^{2+} in tourmaline dictated by structural stability: insights from a schorl with formula $Na^{Y}(Fe^{2+}{}_2Al)^{Z}(Al_5Fe^{2+})(Si_6O_{18})(BO_3)_3(OH)_3(OH,F)$ from Seagull batholith (Yukon Territory, Canada)

Giovanni B. Andreozzi[1] · Ferdinando Bosi[1] · Beatrice Celata[1] · Luca S. Capizzi[1] · Vincenzo Stagno[1] · Christopher E. Beckett-Brown[2]

Received: 21 February 2020 / Accepted: 23 April 2020 / Published online: 7 May 2020

Abstract

A black tourmaline sample from Seagull batholith (Yukon Territory, Canada) was established to be a schorl with concentrations of Fe^{2+} among the highest currently found in nature (FeO_{tot} ~ 18 wt.% and Fe^{2+} ~ 100% of Fe_{tot}) on the basis of a multi-analytical characterization through Mössbauer spectroscopy, electron microprobe, Laser-Ablation Inductively-Coupled-Plasma Mass-Spectrometry and single-crystal X-ray diffraction. From the crystal-chemical analysis, the following empirical formula is proposed: $^{X}(Na_{0.74}\square_{0.24}K_{0.01}Ca_{0.01})_{\Sigma1.00}{}^{Y}(Fe^{2+}{}_{2.05}Al_{0.92}Ti_{0.02}Mn_{0.01}Zn_{0.01})_{\Sigma3.00}{}^{Z}(Al_{5.41}Fe^{2+}{}_{0.53}Mg_{0.06})_{\Sigma6.00}(Si_6O_{18})(BO_3)_3{}^{V}(OH)_3{}^{W}[(OH)_{0.46}F_{0.41}O_{0.13}]_{\Sigma1.00}$, which can be approximated as $Na^{Y}(Fe^{2+}{}_2Al)^{Z}(Al_5Fe^{2+})(Si_6O_{18})(BO_3)_3(OH)_3(OH,F)$. Compared to the formula of the ideal *ordered* schorl, $Na^{Y}(Fe^{2+}{}_3)^{Z}(Al_6)(Si_6O_{18})(BO_3)_3(OH)_3(OH)$, the studied sample has a partial disorder of Fe^{2+} across the *Y* and the *Z* sites that can be expressed by the intracrystalline order–disorder reaction $^{Y}Al + {}^{Z}Fe^{2+} \rightarrow {}^{Y}Fe^{2+} + {}^{Z}Al$. Such a partial cation disorder must be invoked to explain tourmaline structural stability because an ideal ordered schorl results in a large misfit between the $< {}^{Y}Fe^{2+}–O >$ and $< {}^{Z}Al^{3+}–O >$ mean bond lengths (that is, between the YO_6 and ZO_6 polyhedra). This misfit is reduced by introducing Al at *Y* (i.e., through the $< Y–O >$ shortening) and Fe^{2+} at *Z* (i.e., through the $< Z–O >$ lengthening). The result is that in tourmaline the site distribution of high Fe^{2+} concentrations is dictated by long-range structural constraints.

Keywords Tourmaline · Schorl · Mössbauer spectroscopy · Electron microprobe · Laser-ablation inductively-coupled-plasma mass-spectrometry · Single-crystal X-ray diffraction

Introduction

Tourmaline is the most common and earliest boron mineral formed on Earth, recently gaining an interest from the geoscience community (Grew et al. 2016; Dutrow and Henry 2018; Henry and Dutrow 2018). The importance of tourmaline as a powerful geological tool for probing *P–T–X* conditions at all crustal levels in the Earth, resides in its very large *P–T* stability field, common occurrence, and negligible intra-volume element diffusion rates (e.g., Henry and Dutrow 1996; van Hinsberg and Schumacher 2007). Moreover, due to its complex crystal chemistry, which allows a large number of chemical substitutions (e.g., Henry and Dutrow 1996, 2018; Bosi 2018), tourmaline is extremely sensitive to its chemical environment and it is, therefore, valuable as both a petrogenetic and provenance indicator (e.g., Henry and Dutrow 1992, 1996; Dutrow and Henry 2011; van Hinsberg et al. 2011a; Bosi et al. 2018a, 2019a; Ertl et al. 2008, 2012, 2018; Ahmadi et al. 2019; Sipahi 2019).

The tourmaline general chemical formula can be written as $XY_3Z_6T_6O_{18}(BO_3)_3V_3W$, where $X = Na^+, K^+, Ca^{2+}, \square$

Electronic supplementary material The online version of this article (https://doi.org/10.1007/s00269-020-01094-7) contains supplementary material, which is available to authorized users.

✉ Giovanni B. Andreozzi
gianni.andreozzi@uniroma1.it

[1] Dipartimento di Scienze della Terra, Sapienza Università di Roma, Piazzale Aldo Moro 5, 00185 Rome, Italy

[2] Harquail School of Earth Sciences, Laurentian University, Sudbury, ON, Canada

(= vacancy); Y = Al^{3+}, Fe^{3+}, Cr^{3+}, V^{3+}, Mg^{2+}, Fe^{2+}, Mn^{2+}, Zn^{2+}, Li^{+}, Ti^{4+}, □; Z = Al^{3+}, Fe^{3+}, Cr^{3+}, V^{3+}, Mg^{2+}, Fe^{2+}; T = Si^{4+}, Al^{3+}, B^{3+}; B = B^{3+}; V = $(OH)^{-}$, O^{2-}; W = $(OH)^{-}$, F^{-}, O^{2-}. The letters X, Y, Z, T and B represent groups of cations accommodated at the $^{[9]}X$, $^{[6]}Y$, $^{[6]}Z$, $^{[4]}T$ and $^{[3]}B$ crystallographic sites (identified with *italicized* letters); the letters V and W represent groups of anions accommodated at the $^{[3]}$O(3) and $^{[3]}$O(1) crystallographic sites, respectively. The H atoms occupy the H(3) and H(1) sites, which are related to O(3) and O(1), respectively. It is worth mentioning that, unlike amphibole or spinel, the structural and the chemical formula of tourmaline coincide: each crystallographic site in the structural formula matches a (non-italicized) letter in the chemical formula (Bosi et al. 2019b).

Tourmaline-supergroup minerals are currently classified into three groups based on the *X*-site occupancy: vacant, alkali and calcic (Henry et al. 2011). The *X*-site occupancy is usually related to both paragenesis and crystallization conditions of the rock in which tourmaline crystallized, and these relations may be used to reconstruct the host-rock thermal history (Henry and Dutrow 1996; van Hinsberg et al. 2011a, b, 2017; Dutrow and Henry 2018; Bosi et al. 2018a, 2019a). A further level of classification into subgroups is based on charge arrangements at the *Y* and *Z* sites, where small cations such as Al and Mg and relatively larger cations such as Fe^{2+} can be accommodated.

Using a large set of structural data, Bosi and Lucchesi (2007) presented a structural-stability field for tourmaline as a function of < *Y*–O > and < *Z*–O > mean bond lengths. The endpoints of this field indicate that the tourmaline structure can tolerate only a limited mismatch in dimensions between < *Y*–O > and < *Z*-O > (i.e., their difference, $\Delta_{(Y-Z)}$ = < *Y*–O > – < *Z*–O > , should be smaller than 0.15 Å). The empirical validation of the occurrence of a long-range structural constraint and its effect on the occupancy of *Y* and *Z* sites are of particular interest. In fact, cation ordering in tourmaline structure may be exploited for geothermometric purposes (e.g., Henry and Dutrow 1992; Ertl et al. 2008; Filip et al. 2012; Bosi et al. 2016a, b; Ertl et al. 2018), while its variation can affect tourmaline physical properties, such as intrinsic dipole moment (Kim et al. 2018) and bulk moduli (Berryman et al. 2019). The possibility of Fe^{2+} to partially disorder across the *Y* and the *Z* sites, in particular, has been deeply investigated and largely discussed in several papers (see for example Andreozzi et al. 2008; Bosi and Andreozzi 2013, and references therein).

In the present study, a natural schorl with Fe^{2+} concentrations very close to that of schorlitic end-members was studied with an inclusive, multi-analytical approach with the aim to confirm that the crystal-chemical behavior of Fe^{2+} in tourmaline is controlled by structural stability requirements.

Material and experimental methods

The sample used for this study is a black tourmaline from a quartz-tourmaline orbicule found in the leucogranites of the Seagull batholith in the Yukon Territory, Canada (Fig. 1). According to Sinclair and Richardson (1992), the orbicules are considered to have developed during the final crystallization stages in which a hydrous melt/fluid (enriched in B, F, Cl and Fe) separated from a peraluminous granite, and tourmalines from the Seagull batholith are schorl with up to ~ 20 wt.% FeO and normalized Fe^{2+} cations up to 2.78 atoms per formula unit (apfu). To the best of our knowledge, these Fe^{2+} concentrations are the highest found in natural schorl so far.

Fig. 1 Quartz-tourmaline pegmatitic orbicules included in leucogranites from Seagull batholith (Yukon Territory, Canada). Black tourmaline crystals up to 2-cm large are visible in the right inset

In the present study, the Fe oxidation state was obtained by ^{57}Fe Mössbauer Spectroscopy (MS); the chemical composition was obtained by using Electron MicroProbe (EMP) for major and minor elements and Laser-Ablation Inductively-Coupled-Plasma Mass-Spectrometry (LA-ICP-MS) for trace elements (including Li) and B; crystal-structure details were obtained by Structure REFinement (SREF) of X-ray single-crystal diffraction data.

MS

A fragment of the black Seagull tourmaline was ground under ethanol with an agate mortar, and 15 mg of the recovered fine powder was packed to make a disk of 10 mm of diameter. The absorber was then loaded in a Plexiglas® sample holder, and measurements were performed using a conventional spectrometer with a ^{57}Co source of 0.99 GBq (25 mCi) embedded in a Rh matrix available at the Earth Sciences Department, Sapienza University of Rome (Italy). The spectrum was collected in transmission mode, at room temperature and at velocities between –4 to + mm/s, and recorded in a multichannel analyzer with 512 channels. The velocity was calibrated with a 25-μm thick α-iron foil. The obtained absorption spectrum was fitted to Lorentzian lineshapes using the RECOIL 1.04 fitting program (Lagarec and Rancourt 1998), with results reported in Table 1.

EMP

Electron microprobe analysis for the Seagull tourmaline sample was obtained using a wavelength-dispersive spectrometer (WDS mode) with a Cameca SX50 instrument at the "Istituto di Geologia Ambientale e Geoingegneria (Rome, Italy), CNR", operating at an accelerating potential of 15 kV, with a 15 nA current and a 10 μm beam diameter. Minerals and synthetic compounds were used as standards: wollastonite (Si, Ca), magnetite (Fe), rutile (Ti), corundum (Al), vanadinite (V), fluorphlogopite (F), periclase (Mg), jadeite (Na), orthoclase (K), sphalerite (Zn), rhodonite (Mn), metallic Cr, Ni and Cu. The PAP correction procedure for quantitative electron probe microanalysis was applied (Pouchou and Pichoir 1991). Results are reported in Table 2 and represent the mean values of 10 spot analyses across the crystal used for SREF study. Vanadium, Cr, Ni and Cu were below their respective detection limits (0.03 wt%) in the studied sample.

Table 1 Room temperature ^{57}Fe Mössbauer parameters for Seagull schorl from Yukon Territory (Canada)

χ^2	δ	ΔE_Q	Γ	% Area	Assignment
0.75	1.10	2.43	0.31	26	$^{Y}Fe^{2+}$
	1.11	2.11	0.31	36	$^{Y}Fe^{2+}$
	1.11	1.69	0.30	13	$^{Y}Fe^{2+}$
	1.08	1.20	0.46	25	$^{Z}Fe^{2+}$

Centroid shift (δ) in mm/s relative to α-Fe foil; errors are estimated no less than ± 0.02 mm/s for δ, quadrupole splitting (ΔE_Q), and peak width (Γ), and no less than ± 3% for doublets areas

LA-ICP-MS

In-situ trace-element and boron analyses were collected using Laser-Ablation Inductively-Coupled-Plasma mass-spectrometry at Laurentian University (Canada). Samples were ablated using Resonetic Resolution M-50 coupled to a Thermo Electron XSeries II quadrupole ICP-MS. A 193 nm argon fluoride excimer laser was operated at a rate of 8 Hz. Line scans were completed using a 40 μm beam width and a scan speed of 20 μm/s with a measured fluence of ~ 3 j/cm^2. Line scans were utilized to test for chemical zonation, which in turn was not present. Dwell times for rare-earth elements were increased to 15 ms from 10 ms (for other trace elements) to improve detection limits. External reference materials include: (1) NIST 610 (Jochum et al. 2011), (2) NIST 612 (Jochum et al., 2011) and (3) BHVO2G (Raczek et al. 2001). Standards were ablated every 10–15 analyses of the unknowns. Drift correction was applied using the baseline reduction scheme in IOLITE (Paton et al. 2011). Reference standards were utilized to assess the accuracy of the analyses. Results are reported in Table 3,

Table 2 Chemical composition of Seagull schorl from Yukon Territory (Canada)

Oxides	wt.%	Ions	apfu
SiO_2	34.79 (35)	Si	5.998
TiO_2	0.13 (3)	Ti^{4+}	0.016
B_2O_3[a]	10.08	B	3.000
Al_2O_3	31.18 (31)	Al	6.334
FeO[b]	17.91 (22)	Fe^{2+}	2.582
MgO	0.23 (22)	Mg	0.058
MnO	0.04 (3)	Mn^{2+}	0.006
ZnO	0.05 (5)	Zn	0.006
CaO	0.04 (6)	Ca	0.008
Na_2O	2.22 (5)	Na	0.741
K_2O	0.04 (1)	K	0.010
F	0.75 (12)	F	0.409
H_2O[c]	3.01	(OH)	3.463
–O≡F	−0.32		
Total	100.15		

Uncertainties for oxides and fluorine (in brackets) are standard deviation of 10 EMP spots across the crystal used for SREF study. Number of ions normalized to 31 (O, OH, F)

[a]Calculated by stoichiometry, in agreement with LA-ICP-MS results for B

[b]According to Mössbauer spectroscopy results

[c]Calculated by stoichiometry (see text)

together with elemental detection limits, and represent the mean values of 9 analyses across the sample.

SREF

A representative crystal fragment of the Seagull tourmaline was selected for X-ray diffraction measurements on a Bruker KAPPA APEX-II single-crystal diffractometer (Sapienza University of Rome, Earth Sciences Department), equipped with a CCD area detector (6.2 × 6.2 cm active detection area, 512 × 512 pixels) and a graphite-crystal monochromator, using Mo*K*α radiation from a fine-focus sealed X-ray tube. The sample-to-detector distance was 4 cm. A total of 3681 exposures (step = 0.2°, time/step = 20 s) covering a full reciprocal sphere with a redundancy of about 12 was collected. Final unit-cell parameters were refined using the Bruker AXS SAINT program on 9981 reflections with $I > 10\,\sigma(I)$ in the range $5° < 2\theta < 80°$. The associated intensities were processed and corrected for Lorentz and background effects plus polarization, using the APEX2 software program of Bruker AXS. The data were corrected for absorption using a multi-scan method (SADABS). The absorption correction led to a significant improvement in R_{int}. No violation of *R*3*m* symmetry was detected.

Structure refinement was done using the SHELXL-2014 program (Sheldrick 2015). Starting coordinates were taken from Bosi et al. (2015). Variable parameters were: scale factor, extinction coefficient, atom coordinates, site-scattering values (for *X*, *Y* and *Z*) and atomic-displacement factors. Regarding the atomic model refinement, the *X* site was modeled using the Na scattering factor. The occupancies of the *Y* and Z sites were obtained considering the presence of Al versus Fe. The *T*, *B* and anion sites were modeled, respectively, with Si, B and O scattering factors and with a fixed occupancy of 1, because refinement with unconstrained occupancies showed no significant deviations from this value. A final refinement was then performed by modelling the site occupancy of the O(1) site with O and F fixed to the value obtained from the empirical formula (see below). Similar chemical constraints were applied to refine the H(1) and H(3) sites. There were no correlations greater than 0.7 between the parameters at the end of the refinement. Table 4 lists crystal data, data-collection information and refinement details; Table 5 displays the fractional atom coordinates, site occupancy factors and equivalent isotropic-displacement parameters; Table 6 shows selected bond lengths. A CIF file is included in supplemental material.

Results and discussion

Chemical composition and iron speciation

The black tourmaline sample from Seagull batholith (Yukon Territory, Canada) is chemically homogeneous and was

Table 3 Boron and trace-elements contents of Seagull schorl from Yukon Territory (Canada)

Elements	Detection limit (ppm)	Average value (ppm)
^{7}Li	50	bdl
^{9}Be	50	bdl
^{11}B	25	33,725 (1973)
^{31}P	15	bdl
^{33}S	100	bdl
^{39}K	5	483 (39)
^{45}Sc	0.5	84 (14)
^{47}Ti	4	2538 (812)
^{51}V	0.8	3 (2)
^{52}Cr	1.5	bdl
^{55}Mn	1	543 (22)
^{59}Co	0.1	0.93 (0.21)
^{60}Ni	1.5	bdl
^{65}Cu	1.5	16 (9)
^{66}Zn	1	349 (30)
^{69}Ga	0.5	139 (8)
^{72}Ge	0.5	5.8 (0.5)
^{75}As	2	69 (15)
^{85}Rb	0.2	bdl
^{88}Sr	0.02	5 (1)
^{89}Y	0.02	1.2 (0.7)
^{90}Zr	0.04	1.0 (0.4)
^{93}Nb	0.05	8 (4)
^{95}Mo	0.25	bdl
^{115}In	0.01	2.3 (0.6)
^{118}Sn	0.1	40 (15)
^{121}Sb	0.05	1.4 (0.7)
^{139}La	0.01	4 (1)
^{140}Ce	0.01	9 (3)
^{141}Pr	0.02	1.0 (0.3)
^{146}Nd	0.15	3 (1)
^{147}Sm	0.20	0.5 (0.2)
^{153}Eu	0.05	bdl
^{157}Gd	0.10	0.4 (0.2)
^{159}Tb	0.02	0.07 (0.05)
^{163}Dy	0.15	0.4 (0.2)
^{165}Ho	0.03	0.08 (0.04)
^{166}Er	0.08	0.2 (0.1)
^{169}Tm	0.02	0.04 (0.03)
^{172}Yb	0.07	0.3 (0.2)
^{175}Lu	0.03	bdl
^{178}Hf	0.10	bdl
^{208}Pb	0.30	8 (4)
^{232}Th	0.01	0.2 (0.1)
^{238}U	0.05	0.3 (0.2)

Data from LA-ICP-MS, average of 9 analyses across the sample
bdl below detection limit

Table 4 Single-crystal X-ray diffraction data details for Seagull schorl from Yukon Territory (Canada)

Crystal sizes (mm)	0.20 × 0.20 × 0.24
a (Å)	15.9957 (3)
c (Å)	7.1863 (2)
V (Å^3)	1592.36 (7)
Range for data collection, 2θ (°)	6–80
Reciprocal space range *hkl*	$-23 \le h \le 25$ $-27 \le k \le 28$ $-12 \le l \le 11$
Total number of frames	3681
Set of reflections	13,875
Unique reflections, R_{int} (%)	2181, 1.96
Redundancy	12
Absorption correction method	SADABS
Refinement method	Full-matrix last-squares on F^2
Structural refinement program	SHELXL
Extinction coefficient	0.00037 (12)
Flack parameter	0.04 (1)
*wR*2 (%)	3.44
*R*1 (%) all data	1.53
*R*1 (%) for $I > 2\sigma(I)$	1.47
GooF	1.054
Largest diff. peak and hole (± e$^-$/Å^3)	−0.65 and 1.08

R_{int} = merging residual value; *R*1 = discrepancy index, calculated from *F*-data; *wR*2 = weighted discrepancy index, calculated from F^2-data; GooF = goodness of fit; Diff. Peaks = maximum and minimum residual electron density. Radiation, Mo*K*α = 0.71073 Å. Data collection temperature = 293 K. Space group *R*3*m*; *Z* = 3

established to be a schorl (see below) with concentrations of Fe^{2+} among the highest currently found in nature (FeO_{tot} ~ 18 wt.%, Table 2). The Mössbauer absorption spectrum of the Seagull tourmaline shows two dominant absorptions between –1 and +3 mm/s (Fig. 2). The spectrum was deconvoluted using Lorentzian doublets in agreement with models already used in the existing literature (Andreozzi et al. 2008; Bosi et al. 2019b). Accordingly, a model with five doublets was initially adopted and their hyperfine parameters were tentatively refined. Four doublets gave center shift (δ) values around 1.10(2) mm/s and were assigned to $^{[6]}Fe^{2+}$. They are distinguished by their quadrupole splitting (ΔE_Q) values: the first three doublets, conventionally labelled *Y*1, *Y*2 and *Y*3, have ΔE_Q = 2.43(9), 2.11(6), 1.69(11) were interpreted as Fe^{2+} at the *Y* sites with different nearest and next-nearest neighbor coordination environments. The fourth Fe^{2+} doublet, which has ΔE_Q = 1.20(5) mm/s was interpreted as $^{[6]}Fe^{2+}$ in a different chemical environment (or crystallographic-site symmetry) from the *Y* sites, that is Fe^{2+} at the *Z* site. This interpretation is in agreement with the model described in Andreozzi et al. (2008) and Bosi et al. (2015). A potential fifth doublet, centered around 0.3 mm/s and representing $^{[6]}Fe^{3+}$, was quantified to be ≤ 2% of the Fe_{tot}, but its area was smaller than the experimental uncertainty (± 3%) and its hyperfine parameters could not be refined. The contribution of $^{[6]}Fe^{3+}$ was therefore considered to be negligible and all the Fe was eventually considered as $^{[6]}Fe^{2+}$ (Table 1). Notably, the same conclusions were also obtained by Sinclair and Richardson (1992). Concerning site distribution of Fe^{2+}, the absorption doublet assigned to $^{Z}Fe^{2+}$ was quantified at 25(5)% of the Fe_{tot}, which corresponds to 0.65(13) apfu and converges to $^{Z}Fe^{2+}$ obtained by SREF data (see below).

Table 5 Fractional atom coordinates (*x*,*y*,*z*), site occupancy factors (s.o.f.) and equivalent-isotropic (U_{eq}) and isotropic (U_{iso}) displacement parameters (in Å^2) for Seagull schorl from Yukon Territory (Canada)

Site	*x*	*y*	*z*	U_{eq}	s.o.f
X	0	0	0.2289 (3)	0.0226 (6)	$Na_{0.781\ (9)}$
Y	0.12556 (2)	0.06278 (2)	0.62788 (6)	0.00894 (8)	$Fe_{0.697\ (4)}\ Al_{0.303\ (4)}$
Z	0.29881 (2)	0.26176 (2)	0.61151 (6)	0.00607 (9)	$Al_{0.912\ (2)}\ Fe_{0.088\ (2)}$
B	0.11023 (6)	0.22046 (13)	0.4559 (2)	0.0072 (2)	$B_{1.00}$
T	0.19178 (2)	0.18983 (2)	0	0.00519 (7)	$Si_{1.00}$
O(1) (≡W)	0	0	0.7825 (4)	0.0342 (7)	$O_{0.5912}\ F_{0.4088}$
O(2)	0.06155 (5)	0.12311 (9)	0.48594 (19)	0.0139 (2)	$O_{1.00}$
O(3) (≡V)	0.26873 (11)	0.13437 (5)	0.51074 (17)	0.0130 (2)	$O_{1.00}$
O(4)	0.09294 (5)	0.18588 (9)	0.06854 (16)	0.0093 (2)	$O_{1.00}$
O(5)	0.18616 (10)	0.09308 (5)	0.09067 (16)	0.00946 (19)	$O_{1.00}$
O(6)	0.19777 (6)	0.18768 (6)	0.77707 (12)	0.00805 (14)	$O_{1.00}$
O(7)	0.28452 (6)	0.28502 (6)	0.07988 (11)	0.00782 (13)	$O_{1.00}$
O(8)	0.20964 (6)	0.27039 (6)	0.44196 (13)	0.00966 (14)	$O_{1.00}$
H(1)	0	0	0.916 (4)	0.041*	$H_{0.5912}$
H(3)	0.260 (2)	0.1299 (10)	0.383 (3)	0.016*	$H_{1.00}$

*U_{iso}; H(1) and H(3) hydrogen atoms were constrained to have a U_{iso} 1.2 times the U_{eq} value of the O(1) and O(3) oxygen atoms, respectively

Table 6 Selected bond distances (Å) for Seagull schorl from Yukon Territory (Canada)

Bond distance - Value (Å)	Bond distance - Value (Å)	Bond distance - Value (Å)	Bond distance - Value (Å)
B-O(2)	1.366 (2)	*Y*–O(2)^{B} (× 2)	2.0020 (8)
B-O(8)^{A} (× 2)	1.3807 (13)	*Y*–O(6)^{C} (× 2)	2.0414 (9)
< *B*-O >	1.376	*Y*–O(1)	2.0640 (15)
		Y–O(3)	2.1546 (15)
*T**-O(6)	1.6063 (9)	< *Y*–O >	2.051
T-O(7)	1.6093 (8)		
T-O(4)	1.6267 (5)	*Z*-O(6)	1.8753 (9)
T-O(5)	1.6397 (5)	*Z*-O(7)^{E}	1.8901 (8)
< *T*-O >	1.621	*Z*-O(8)^{E}	1.8910 (9)
		Z-O(8)	1.9326 (9)
X-O(2)^{B,F} (× 3)	2.514 (2)	*Z*-O(7)^{D}	1.9710 (9)
X-O(5)^{B,F} (× 3)	2.7635 (15)	*Z*-O(3)	1.9819 (6)
X-O(4)^{B,F} (× 3)	2.8210 (15)	< *Z*-O >	1.924
< *X*-O >	2.700		

Standard uncertainty in parentheses. Superscript letters: A = (*y* – *x*, *y*, *z*); B = (*y* – *x*, – *x*, *z*); C = (*x*, *x* – *y*, *z*); D = (*y* – *x* + 1/3, – *x* + 2/3, *z* + 2/3); E = (–*y* + 2/3, *x* – *y* + 1/3, *z* + 1/3); F = (–*y*, *x* – *y*, *z*). Transformations relate coordinates to those of Table 5

*T** = positioned in adjacent unit cell

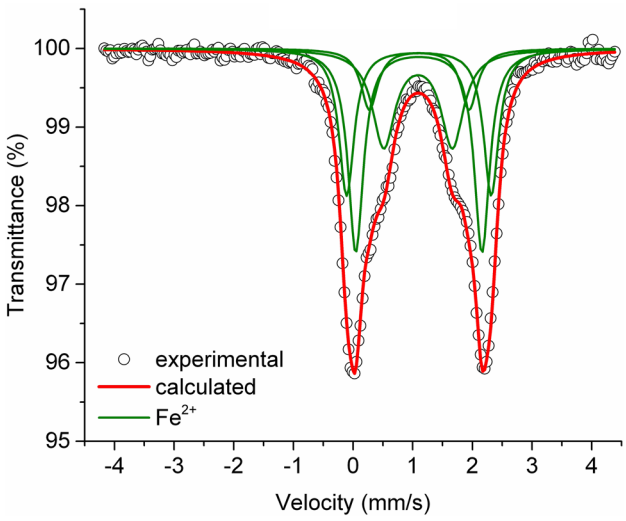

Fig. 2 Room temperature ^{57}Fe Mössbauer spectrum for Seagull schorl from Yukon Territory (Canada). Experimental spectrum (exp) is represented by open circles, calculated spectrum (calc) by thick red curve (reduced $\chi^2 = 0.68$). Lorentzian absorption doublets assigned to $^{[6]}Fe^{2+}$ are represented by thin green lines

Site populations

The Li content was considered negligible for crystal-chemical purposes because it is below the detection limit of LA-ICP-MS analysis. The B content was assumed to be stoichiometric (B = 3.00 apfu corresponding to B_2O_3 = 10.08 wt.%) as corresponding to the LA-ICP-MS results, within the experimental uncertainty (Table 3). A stoichiometric B content is further supported by the SREF results (Tables 5, 6): the values of the *B*- and *T*-site occupancy factors and the < *B*–O > and < *T*–O > distances are effectively consistent with the *B* and *T* sites fully occupied by B and Si, respectively (e.g., Bosi and Lucchesi 2007). Based on MS results, the oxidation state of all Fe atoms was considered exclusively +2. The (OH) contents and the atomic fractions were then calculated by charge balance under the assumption of (T + Y + Z) = 15.00 apfu and 31 anions. The excellent agreement between the number of electrons per formula unit (epfu) derived from chemistry and from SREF (258.3 epfu *versus* 258.6 epfu, respectively) supports the above stoichiometric assumptions.

With regard to the site populations at *X*, *B*, *T*, O(3) (≡ V) and O(1) (≡ W), the standard site preference suggested for tourmaline (e.g., Henry et al. 2011) were actually satisfied, while the *Y* and *Z* site populations were optimized according to the procedure of Bosi et al. (2017) and by fixing the minor elements Ti^{4+}, Mn^{2+} and Zn at *Y*. The robustness of this optimized cation distribution was successively confirmed by the procedure of Wright et al. (2000) in which the default setting was assumed, but the chemical variability was constrained by electroneutrality. The resulting empirical formula for the Seagull tourmaline is:

$^{X}(Na_{0.74}\square_{0.24}K_{0.01}Ca_{0.01})_{\Sigma 1.00}{}^{Y}(Fe^{2+}{}_{2.05}Al_{0.92}Ti_{0.02}Mn_{0.01}Zn_{0.01})_{\Sigma 3.00}{}^{Z}(Al_{5.41}Fe^{2+}{}_{0.53}Mg_{0.06})_{\Sigma 6.00}(Si_6O_{18})(BO_3)_3{}^{V}(OH)_3{}^{W}[(OH)_{0.46}F_{0.41}O_{0.13}]_{\Sigma 1.00}$.

The refined site-scattering values and those calculated from the optimized site-populations are in excellent

agreement (Table 7). It is worth noting the occurrence at *Z* site of significant amounts of Fe^{2+} (0.53 apfu), which is a cation heavier than Al and it is thus required to justify the refined *Z*-site scattering value (*Z*-m.a.n, where m.a.n. is the mean atomic number) of 14.14(3), considerably larger than the expected value for a *Z* site fully occupied by Al (*Z*-m.a.n = 13). Such a cation distribution is also corroborated by the refined < *Z*–O > value (1.924 Å), which is larger than the typical < *Z*–O > values observed for a *Z* site fully occupied by Al (1.902–1.913 Å; Bosi and Andreozzi 2013) and reflects the presence of cations larger than Al at the *Z* site (as, for example, Fe^{2+}). Finally, as previously highlighted, the amounts of Fe^{2+} at *Z* retrieved by SREF (0.53 apfu) are consistent with the absorption area of the MS doublet assigned to $^{Z}Fe^{2+}$ (Table 1), which corresponds to ~ 0.65(13) apfu.

Influence of the tourmaline structural stability on the Al-Fe^{2+} order–disorder

The empirical formula of the Seagull tourmaline is consistent with a tourmaline belonging to the alkali group (Henry et al. 2011): Na-dominant at the X position of the tourmaline general chemical formula and (OH)-dominant at W (OH > F). The Y and Z positions are dominated by Fe^{2+} and Al, respectively. In accord with the IMA-CNMNC rules (Bosi et al. 2019d), the end-member formula is $^{X}(Na)^{Y}(Fe^{2+})_3{}^{Z}(Al)_6(Si_6O_{18})(BO_3)_3(OH)_3(OH)$, corresponding to schorl (Henry et al. 2011). By our most comprehensive understandings, the Seagull schorl is the Fe^{2+}-richest schorl investigated by SREF thus far, even richer than the fluor-schorl from Steinberg, Germany, for which FeO_{tot} = 16.5 wt.% and $Fe^{2+} \leq 96\%$ of Fe_{tot} (Ertl et al. 2016).

The composition of the studied schorl can be approximated as $Na^{Y}(Fe^{2+}{}_2Al)^{Z}(Al_5Fe^{2+})(Si_6O_{18})(BO_3)_3(OH)_3(OH,F)$. With respect to the ideal *ordered* schorl (Fe^{2+} ordered at *Y* and Al at *Z*, see above), the observed partial disorder of Fe^{2+} over the *Y* and the *Z* sites (68% and 9% atoms/site, respectively) can be explained by the intracrystalline order–disorder reaction $^{Y}Al + {}^{Z}Fe^{2+} \rightarrow {}^{Y}Fe^{2+} + {}^{Z}Al$, which is needed to satisfy the long-range structural stability of tourmaline (Bosi 2018). In fact, in the ideal ordered schorl the expected difference between the < $^{Y}Fe^{2+}$–O > and < ^{Z}Al–O > would be $\Delta_{(Y-Z)}$ = 0.232 Å [< $^{Y}Fe^{2+}$–O > = 2.136(1) Å and < ^{Z}Al–O > = 1.904(3) Å, calculated from the ionic radii of Bosi (2018)], that is too large and inconsistent with the structural stability limits of the tourmaline supergroup minerals: $\Delta_{(Y-Z)}$ less than 0.15 Å [as proposed by Bosi and Lucchesi (2007) and successively confirmed by Bosi (2018) using 322 SREF data sets]. Consequently, the structure of the ordered schorl would be unstable (Fig. 3). In the studied schorl, the misfit between < *Y*–O > and < *Z*–O > is reduced to 0.127 Å by the reaction $^{Y}Al + {}^{Z}Fe^{2+} \rightarrow {}^{Y}Fe^{2+} + {}^{Z}Al$, which mitigates the potential misfit by shortening < *Y*–O > up to 2.051 Å (introducing ^{Y}Al) and increasing < *Z*–O > up to 1.924 Å (introducing $^{Z}Fe^{2+}$). Therefore, the data are consistent with the partial disordering of significant amounts of Fe^{2+} into the Z sites as a mechanism to establish long-range structural stability (Fig. 3).

The site redistribution of Fe–Mg–Al over the *Y* and *Z* sites was experimentally investigated at high temperature for schorl, dravite, Fe-bearing oxy-dravite, lucchesiite and Fe-rich fluor-elbaite by Filip et al. (2012), Bosi et al. (2016a,b, 2018b, 2019c). These studies, conducted at both oxidizing and reducing conditions, showed significant Fe–Mg–Al intersite exchanges when Fe-bearing tourmalines were heated up to 700–800 °C, with Fe always involved in the disordering process (up to 0.37 apfu of ^{Z}Fe for schorl and lucchesiite). Although the possibility of a geothermometric exploitation of tourmaline intersite exchanges is encouraging, the present results (with $^{Z}Fe^{2+}$ = 0.53 apfu) suggest adopting some precautions, at least for very high Fe contents, due to the important role of the long-range structural constraints on Fe^{2+} site distribution.

Conclusions

The comprehensive multi-analytical approach of this study of a schorl sample from Seagull batholith (Yukon Territory, Canada) constrains the crystal-chemical behavior of Fe^{2+} in tourmaline. The studied sample is the Fe^{2+}-richest schorl with SREF data known in the literature.

From a crystal-chemical viewpoint, a partial disorder of Fe^{2+} over the *Y* and *Z* sites was observed, and this is required for the long-range structural constraints to be

Table 7 Site-scattering values and optimized site-populations for Seagull schorl from Yukon Territory (Canada)

Site	Refined site-scattering (epfu)	Optimized site-population (apfu)	Calculated site-scattering (epfu)
X	8.59 (8)	0.74 Na + 0.24 □ + 0.01 K + 0.01 Ca	8.49
Y	66.18 (26)	2.05 Fe^{2+} + 0.92 Al + 0.02 Ti^{4+} + 0.01 Mn^{2+} + 0.01 Zn	66.01
Z	84.86 (17)	5.41 Al + 0.53 Fe^{2+} + 0.06 Mg	84.82

epfu electrons per formula unit, *apfu* atoms per formula unit

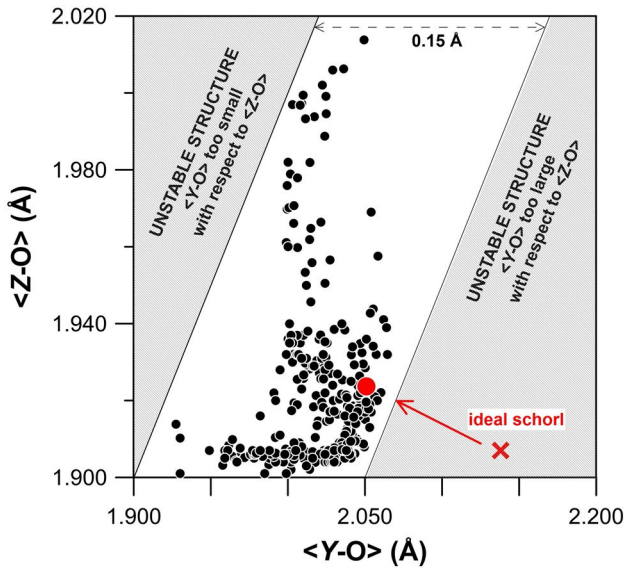

Fig. 3 Relation between < *Z*–O > and < *Y*–O > showing the structural-stability limits for tourmaline minerals. Solid diagonal lines: left = ratio 1:1 between < *Z*–O > and < *Y*–O > ; right = ratio 1:1 shifted by 0.15 Å. The full red circle represents the partially disordered Seagull schorl from Yukon Territory (Canada); the red cross is the ideal ordered schorl; black dots represents 322 data sets with SREF. Modified from Bosi (2018)

fulfilled. Similar arguments were applied to explain the observed partial disorder of Mg over *Y* and *Z* for dravite and fluor-dravite, as well as the failure in synthesizing the tsilaisite end-member composition (Bosi and Lucchesi 2007; Clark et al. 2011; Bosi et al. 2012; Bosi 2018). For tourmaline to be stable, the 3-D framework of ZO_6 octahedra must be able to accommodate the structural islands made of (XO_9 + YO_6 + BO_3 + TO_4) polyhedra. With *Z* site fully occupied by Al, very high amounts (>> 2 apfu) of Mg^{2+}, Fe^{2+} and Mn^{2+} ordered at the *Y* site would make tourmaline unstable, because the resulting difference between < *Y*–O > and < *Z*–O > would be too large [i.e., $\Delta_{(Y-Z)} > 0.15$ Å]. A partial disorder of Al and R^{2+}-cations over *Y* and *Z* is, therefore, necessary to reduce the misfit between YO_6 and ZO_6 and to guarantee tourmaline structure stability.

Acknowledgements The Seagull schorl was generously made available by Dave Sinclair (Geological Survey of Canada). Funding by the Deep Energy Community of the Deep Carbon Observatory (UCLA Subaward Number 2090 G UA406 to G.B. Andreozzi) and by Sapienza University of Rome (Prog. Università 2017 to V. Stagno and 2018 to F. Bosi) is gratefully acknowledged. The authors sincerely thank the Editor Milan Rieder for his professional handling, and Darrell J. Henry and an anonymous reviewer for their constructive comments that helped to improve the manuscript.

References

Ahmadi S, Tahmasbi Z, Khalaji AA, Zal F (2019) Chemical variations and origin of tourmalines in laleh zar granite of Kerman (Southeast Iran). Period Mineral 88:117–129

Andreozzi GB, Bosi F, Longo M (2008) Linking Mossbauer and structural parameters in elbaite-schorl-dravite tourmalines. Am Mineral 93:658–666

Berryman EJ, Zhang D, Wunder B, Duffy TS (2019) Compressibility of synthetic Mg-Al tourmalines to 60 GPa. Am Mineral 104:1005–1015

Bosi F (2018) Tourmaline crystal chemistry. Am Mineral 103:298–306

Bosi F, Lucchesi S (2007) Crystal chemical relationships in the tourmaline group: structural constraints on chemical variability. Am Mineral 92:1054–1063

Bosi F, Andreozzi GB (2013) A critical comment on Ertl et al. (2012): limitations of Fe^{2+} and Mn^{2+} site occupancy in tourmaline: evidence from Fe^{2+}- and Mn^{2+}-rich tourmaline. Am Mineral 98:2183–2192

Bosi F, Skogby H, Agrosì G, Scandale E (2012) Tsilaisite, $NaMn_3Al_6(Si_6O_{18})(BO_3)_3(OH)_3OH$, a new mineral species of the tourmaline supergroup from Grotta d'Oggi, San Pietro in Campo, island of Elba, Italy. Am Mineral 97:989–994

Bosi F, Andreozzi GB, Hålenius U, Skogby H (2015) Experimental evidence for partial Fe^{2+} disorder at the Y and Z sites of tourmaline: a combined EMP, SREF, MS, IR and OAS study of schorl. Min Mag 79:515–528

Bosi F, Skogby H, Balić-Žunić T (2016a) Thermal stability of extended clusters in dravite: a combined EMP, SREF and FTIR study. Phys Chem Mineral 43:395–407

Bosi F, Skogby H, Hålenius U (2016b) Thermally induced cation redistribution in Fe-bearing oxy-dravite and potential geothermometric implications. Contrib Mineral Petrol 171:47

Bosi F, Reznitskii L, Hålenius U, Skogby H (2017) Crystal chemistry of Al-V-Cr oxy-tourmalines from Sludyanka complex, Lake Baikal, Russia. Eur J Mineral 29:457–472

Bosi F, Naitza S, Skogby H, Secchi F, Conte AM, Cuccuru S, Hålenius U, De La Rosa N, Kristiansson P, Nilsson EJC, Ros L, Andreozzi GB (2018a) Late magmatic controls on the origin of schorlitic and foititic tourmalines from late-Variscan peraluminous granites of the Arbus pluton (SW Sardinia, Italy) Crystal-chemical study and petrological constraints. Lithos 308:395–411

Bosi F, Skogby H, Hålenius U, Ciriotti M (2018b) Experimental cation redistribution in the tourmaline lucchesiite, $CaFe^{2+}{}_3Al_6(Si_6O_{18})(BO_3)_3(OH)_3O$. Phys Chem Mineral 45:621–632

Bosi F, Naitza S, Secchi F, Conte AM, Cuccuru S, Andreozzi GB, Skogby H, Hålenius U (2019a) Petrogenetic controls on the origin of tourmalinite veins from Mandrolisai igneous massif (Central Sardinia, Italy): Insights from tourmaline crystal chemistry. Lithos 342–343:333–344

Bosi F, Biagioni C, Oberti R (2019b) On the chemical identification and classification of minerals. Minerals 9(10):591

Bosi F, Skogby H, Hålenius U (2019c) Thermally induced cation redistribution in fluor-elbaite and Fe-bearing tourmalines. Phys Chem Mineral 46:371–383

Bosi F, Hatert F, Hålenius U, Pasero M, Miyawaki R, Mills SJ (2019d) On the application of the IMA-CNMNC dominant-valency rule to complex mineral compositions. Mineral Mag 83:627–632

Clark CM, Hawthorne FC, Ottolini L (2011) Fluor-dravite, $NaMg_3Al_6Si_6O_{18}(BO_3)_3(OH)_3F$, a new mineral species of the tourmaline group from the Crabtree emerald mine, Mitchell County, North Carolina: description and crystal structure. Can Mineral 49:57–62

Dutrow B, Henry D (2011) Tourmaline: a geologic DVD. Elements 7:301–306

Dutrow B, Henry D (2018) Tourmaline compositions and textures: reflections of the fluid phase. J Geosci 63:99–110

Ertl A, Tillmanns E, Ntaflos T, Francis C, Giester G, Körner W, Hughes JM, Lengauer C, Prem M (2008) Tetrahedrally coordinated boron in Al-rich tourmaline and its relationship to the pressure–temperature conditions of formation. Eur J Mineral 20:881–888

Ertl A, Schuster R, Hughes JM, Ludwig T, Meyer H-P, Finger F, Dyar MD, Ruschel K, Rossman GR, Klötzli U, Brandstätter F, Lengauer CL, Tillmanns E (2012) Li-bearing tourmalines in Variscan pegmatites from the Moldanubian nappes, Lower Austria. Eur J Mineral 24:695–715

Ertl A, Kolitsch U, Dyar MD, Meyer HP, Rossman GR, Henry DJ, Prem M, Ludwig T, Nasdala L, Lengauer CL, Tillmanns E, Niedermayr G (2016) Fluor-schorl, a new member of the tourmaline supergroup, and new data on schorl from the cotype localities. Eur J Mineral 28:163–177

Ertl A, Henry DJ, Tillmanns E (2018) Tetrahedral substitutions in tourmaline: a review. Eur J Mineral 30:465–470

Filip J, Bosi F, Novák M, Skogby H, Tuček J, Čuda J, Wildner M (2012) Iron redox reactions in the tourmaline structure: High-temperature treatment of Fe^{3+}-rich schorl. Geochim Cosmochim Acta 86:239–256

Grew ES, Krivovichev SV, Hazen RM, Hystad G (2016) Evolution of structural complexity in boron minerals. Can Mineral 54:125–143

Henry DJ, Dutrow BL (1992) Tourmaline in a low grade clastic metasedimentary rock: an example of the petrogenetic potential of tourmaline. Contrib Mineral Petrol 112:203–218

Henry DJ, Dutrow BL (1996) Metamorphic tourmaline and its petrologic applications. In: Grew ES, Anovitz LM (eds), Boron: mineralogy, petrology and geochemistry. Rev Mineral Geochem 33:503–557

Henry DJ, Dutrow BL (2018) Tourmaline studies through time: contributions to scientific advancements. J Geosci 63:77–98

Henry DJ, Novák M, Hawthorne FC, Ertl A, Dutrow BL, Uher P, Pezzotta F (2011) Nomenclature of the tourmaline supergroup minerals. Am Mineral 96:895–913

Jochum KP, Weis U, Stoll B, Kuzmin D, Yang Q, Raczek I, Jacob DE, Stracke A, Birbaum K, Frick DA, Günther D, Enzweiler J (2011) Determination of reference values for NIST SRM 610–617 glasses following ISO guidelines. Geostand Geoanal Res 35:397–429

Kim Y, Jong K, Li G, Kim C, Jon Y, Jong C (2018) Numerical simulation of intrinsic dipole moment according to ion substitution and order-disorder reactions in tourmaline. Can Mineral 56:951–965

Lagarec K, Rancourt DG (1998) RECOIL, Mössbauer spectral analysis software for windows (version 1.0). Department of Physics, University of Ottawa, Canada

Paton C, Hellstrom J, Paul B, Woodhead J, Hergt J (2011) Iolite: Freeware for the visualisation and processing of mass spectrometric data. J Anal Atom Spectrom 26:2508–2518

Pouchou JL, Pichoir F (1991) Quantitative analysis of homogeneous or stratified microvolumes applying the model "PAP". In: Heinrich KFJ, Newbury DE (eds) Electron probe quantitation. Plenum, New York, pp 31–75

Raczek I, Stoll B, Hofmann AW, Jochum KP (2001) High-precision trace element data for the USGS reference materials BCR-1, BCR-2, BHVO-1, BHVO-2, AGV-1, AGV-2, DTS-1, DTS-2, GSP-1 and GSP-2 by ID-TIMS and MIC-SSMS. Geostandards Newslett 25:77–86

Sheldrick GM (2015) Crystal structure refinement with SHELXL. Acta Crystallogr C 71:3–8

Sipahi F (2019) Nature of tourmaline formation in quartz porphyry in the E Sakarya zone (NE Turkey): Geochemistry and isotopic approach. Period Mineral 88:333–351

Sinclair WD, Richardson JM (1992) Quartz-tourmaline orbicules in the Seagull Batholith, Yukon Territory. Can Mineral 30:923–935

Wright SE, Foley JA, Hughes JM (2000) Optimization of site occupancies in minerals using quadratic programming. Am Mineral 85:524–531

van Hinsberg VJ, Schumacher JC (2007) Intersector element partitioning in tourmaline: a potentially powerful single crystal thermometer. Contrib Mineral Petrol 153:289–301

van Hinsberg VJ, Henry DJ, Marschall HR (2011a) Tourmaline: an ideal indicator of its host environment. Can Mineral 49:1–16

van Hinsberg VJ, Henry DJ, Dutrow BL (2011b) Tourmaline as a petrologic forensic mineral: a unique recorder of its geologic past. Elements 7:327–332

van Hinsberg VJ, Franz G, Wood BJ (2017) Determining subduction-zone fluid composition using a tourmaline mineral probe. Geochem Persp Let 3:160–169